Controlled Growth and Reliable Thickness-Dependent Properties of Organic–Inorganic Perovskite Platelet Crystal

Lin Niu, Qingsheng Zeng, Jia Shi, Chunxiao Cong, Chunyang Wu, Fucai Liu, Jiadong Zhou, Wei Fu, Qundong Fu, Chuanhong Jin, Ting Yu, Xinfeng Liu, and Zheng Liu**

Organolead halide perovskites (e.g., $CH_3NH_3PbI_3$) have caught tremendous attention for their excellent optoelectronic properties and applications, especially as the active material for solar cells. Perovskite crystal quality and dimension is crucial for the fabrication of high-performance optoelectronic and photovoltaic devices. Herein the controlled synthesis of organolead halide perovskite $CH_3NH_3PbI_3$ nanoplatelets on SiO_2/Si substrates is investigated via a convenient two-step vapor transport deposition technique. The thickness and size of the perovskite can be well-controlled from few-layers to hundred nanometers by altering the synthesis time and temperature. Raman characterizations reveal that the evolutions of Raman peaks are sensitive to the thickness. Furthermore, from the time-resolved photoluminescence measurements, the best optoelectronic performance of the perovskite platelet is attributed with thickness of ≈30 nm to its dominant longest lifetime (≈4.5 ns) of perovskite excitons, which means lower surface traps or defects. This work supplies an alternative to the synthesis of high-quality organic perovskite and their possible optoelectronic applications with the most suitable materials.

1. Introduction

Recently, methyl ammonium lead halides, the structural analogues of the natural perovskites crystal, have received much attention for their good optoelectronic properties.[1–12] Benefited from their optimal band gap (1.5–1.65 eV), high absorption coefficient, long electron/hole diffusion lengths (≈100 nm to ≈1 μm), and good optical and electrical transport properties, this kind of organic-based lead halide perovskites have been employed not only as light absorption materials for solar cells but also in photodetectors, field-effect transistors, light-emitting diodes, superconductors, ferroelectrics, and so forth.[10,13–17] Recent results about the highest solar-to-electric conversions are mainly investigated by using two main compounds: $CH_3NH_3PbI_3$ and $CH_3NH_3PbI_{3-x}Cl_x$, showing minor alterations in halide content.[1,7,18,19] So far, the highest efficiency of organometal perovskite is up to ≈20% demonstrated in lab-scale devices.[20] There are several traditional one-step or two steps methods to prepare organic-based lead halide perovskite films, such as spin-casting, dip coating, and thermal evaporation, which are suitable and low-cost forms to study their optical and electrical properties.[2,7,21] There have been extensive investigations on the perovskite synthesis by using these common methods into varied nanoparticles (0D), nanowires (1D), nanoplatelets (2D), and their fantastic optical and electrical properties, leading to a number of exciting applications in optoelectronics.[22–27] Tiny alterations of the materials' characterizations (size, thickness, roughness, morphology, crystal structure, and so on) may lead to dramatically diverse device performances.[8,28–33] This indicates that it is critical to have fine control over the crystal growth methods and conditions of the organic-based lead halide perovskites.[28,29] By using spin-casting, dip coating, and thermal evaporation, it is benefit to control the appropriate perovskite film thickness and size for the optoelectronic device preparation and measurement. However, the perovskite films acquired by these methods are generally polycrystalline with high roughness and the reduction of perovskite film quality.[2,34] Some groups got high-crystal-quality PbI_2 and perovskite nanoplatelets by physical vapor deposition (PVD) and chemical vapor deposition (CVD) method and sufficiently investigated their good optical properties with different platelet thicknesses.[35–37] However, the utilization and characteristics of 2D nanoarchitectures for many important few-layered perovskite materials are still not very well documented, which are of great importance in fabricating electronic and optoelectronic device due to their compatibility with traditional microfabrication techniques. To the best of our

Dr. L. Niu, Dr. Q. Zeng, Dr. F. Liu, J. Zhou, Dr. W. Fu, Q. Fu, Prof. Z. Liu
Center for Programmable Materials
School of Materials Science & Engineering
Nanyang Technological University
Singapore 639798, Singapore
E-mail: z.liu@ntu.edu.sg

J. Shi, Prof. X. Liu
CAS Key Laboratory of Standardization and Measurement for Nanotechnology, CAS Center for Excellence in Nanoscience
National Center for Nanoscience and Technology
Beijing 100190, P.R. China
E-mail: liuxf@nanoctr.cn

Dr. C. Cong, Prof. T. Yu
School of Physical and Mathematical Sciences
Nanyang Technological University
Singapore 637371, Singapore

Dr. C. Wu, Prof. C. Jin
State Key Laboratory of Silicon Materials and School of Materials Science and Engineering
Zhejiang University
Hangzhou 310027, P. R. China

DOI: 10.1002/adfm.201601392

© 2016 WILEY-VCH Verlag GmbH & Co. KGaA, Weinheim

knowledge, nobody has already reported CVD lead halide perovskite species in 2D platelets on SiO_2 and explore their intelligent applications in optoelectronic devices, especially with their thickness-dependent properties. Herein, to select best PbI_2 growth temperature and time, we well-controlled synthetized lead halide perovskite family nanoplatelets with lateral dimensions from 5 to 30 μm and thicknesses from few layers to several hundred nanometers on SiO_2/Si substrates and even try to control the perovskite thickness within few nanometers. Raman spectroscopy provided the sensitive thickness-dependent Raman peaks evolutions. Further, we investigate the characterizations and mechanism of thickness dependent photoresponse for the perovskite nanoplatelets.

2. Results and Discussion

2.1. Materials Characterizations of the Perovskite Nanoplatelets on SiO_2/Si Substrates

In this work, we demonstrate the vapor phase deposition of 2D triangular or hexagonal perovskite nanoplatelets on SiO_2/Si substrates. The two-step experimental setup is demonstrated in **Figure 1**a. For the synthesis of PbI_2 platelets, we controlled different deposit temperature by both the tube furnace temperature set system within a range from 350 to 380 °C and various SiO_2/Si position placed in the tube corresponding to different tube furnace temperature regions. Finally, we found that the most appropriate setting temperature is 360 °C and the best location of the SiO_2/Si shown as the tube furnace schematic in Figure S1 (Supporting Information). Highly crystalline lead halide PbI_2 platelets are furnished on SiO_2/Si substrates under vacuum with an inert carrier argon gas. After that, the converting reaction was carried out by using gas-phase methyl ammonium halides inserting into PbI_2 nanoplatelets. The optical microscope images in Figure 1b are obtained from the synthesized perovskite nanoplatelets on SiO_2/Si substrates. The typical shape of perovskite nanostructures are regular 2D triangular and hexagonal nanoplatelets (Figure 1b inset) with lateral dimension of about 5–20 μm. The atomic force microscopy (AFM) was carried out to show the morphologies and thickness of 2D perovskite nanoplatelets. As indicated by Figure 1c and Figures S2–S5 (Supporting Information), thickness of 2D perovskite nanoplatelets mainly distributes in 5–300 nm, depending on controlled growth time. Obviously, optical color image shows different colors of perovskite nanoplatelets with similar nanoplate lateral size. The color change with the platelet thickness results from the optical interference between the top surface and bottom surface of perovskite platelet. Optical path difference between the two beams is determined by both the thickness of pervoskite and the angle of incidence light, so that the colors of perovskite crystal

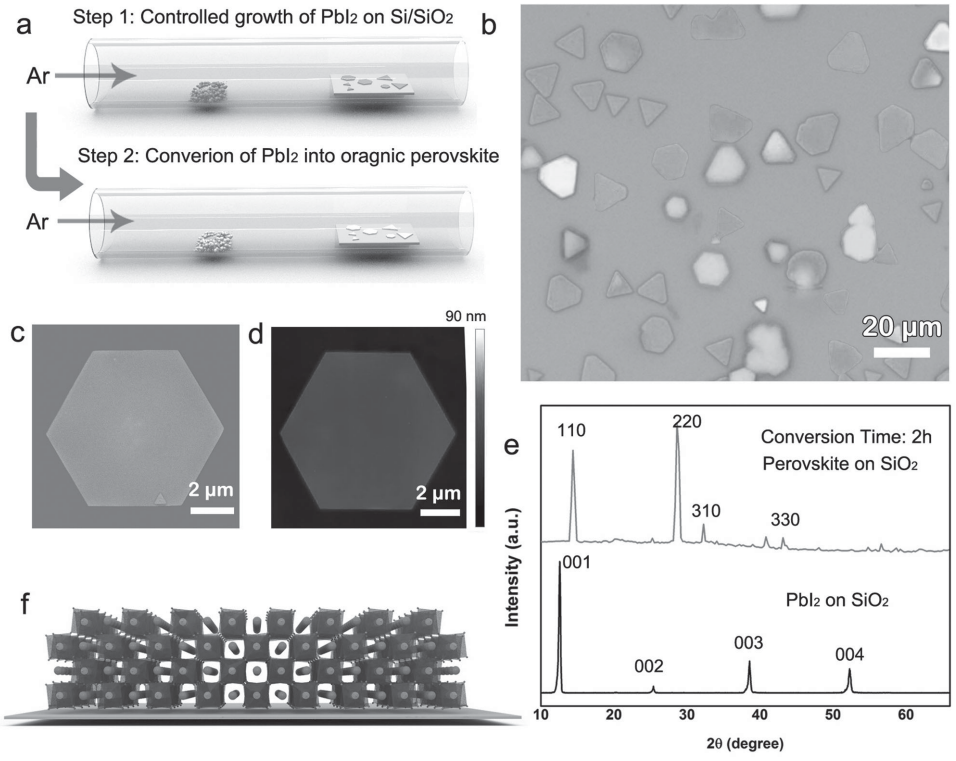

Figure 1. Overall morphologies of the perovskite nanoplatelets on Si/SiO_2 substrate. a) Two-step method for the synthesis of perovskite nanoplatelets. Step 1: Highly crystalline PbI_2 nanoplatelets were grown on Si/SiO_2 substrates via the physical vapor deposition (PVD). Step 2: The PbI_2 crystals were then converted into perovskite, whereby reacting with CH_3NH_3I under vacuum. The morphologies of organic perovskite nanoplatelets on Si/SiO_2 substrates were examined by b) optical microscopy, c) SEM, and d) AFM. e) X-ray diffraction patterns of PbI_2 and perovskite nanoplatelets growth on Si/SiO_2 substrates. The atomic structure of organic perovskite is displayed in (f).

© 2016 WILEY-VCH Verlag GmbH & Co. KGaA, Weinheim

nanoplatelets obtained from the optical images vary depending on the platelet thickness. We have performed the AFM measurements of these nanoplatelets with different optical colors to confirm the dimensional range. The results show the optical colors are highly related to their thickness. As shown in Figure S5 (Supporting Information), the thickness of purple perovskite nanoplate is 5–10 nm, while for dark-blue nanoplatelets, the thickness increases to ≈20 nm. The optical colors of perovskite nanoplatelets gradually become lighter and lighter with the increase of thickness. Optical contrast dependence of thickness provides a facile way to roughly identify the vertical dimensions of perovskite nanoplatelets. We could also use scanning electron microscopy (SEM) and AFM to investigate the quality of perovskite crystal nanoplatelets (Figure 1c,d). Surface morphology of perovskite nanoplatelets are highly smooth and flat as seen in Figures S1 and S3 (Supporting Information), with only ≈1.5 nm surface roughness, suggesting that the high quality of perovskite nanoplatelets was obtained and the perovskite conversion is completed and uniform.

X-ray diffraction (XRD) patterns of PbI_2 and perovskite nanoplatelets also substantiate this claim with hard evidence. At the initial stage after PbI_2 deposition growth on SiO_2/Si substrates, X-ray diffraction patterns of PbI_2 nanoplatelets are shown in Figure 1e. A set of strong peaks at 12.58, 25.4, 38.56, and 52.26, assigned to 001, 002, 003, and 004 of the PbI_2 crystal (space group: P3m 1(164), JCPDS file No. 07-0235), indicating high level of phase purity of hexagon crystal structure of PbI_2 with a highly oriented growth direction along the *c*-axis.[38] The similarity of the lead halide and perovskite structures makes it possible to convert the lead halide solid structure into its perovskite by intercalating methyl ammonium halide molecules. During the conversion revolution, CH_3NH_3I attended the chemical reaction with PbI_2. The methyl ammonium part of this organic molecule $CH_3NH_3^+$ denoted as an orange sphere in the schemes is inserted into the octahedral structure of PbI_2 and located within the center of eight lead halide octahedrons. With the advance of time, the PbI_2 peaks totally disappears at the conversion complete stage (2 h in this work for the perovskite nanoplatelets with the thickness around 200–400 nm), and the pure perovskite were obtained with high crystallinity. The perovskite have been totally converted in these nanoplatelets, owning the characteristic peaks at 14.4, 28.64, 32.26, and 43.15, assigned to (110), (220), (310), and (330) for $CH_3NH_3PbI_3$ perovskite with a tetragonal crystal structure.[39] Figure 1f shows the structure schemes of perovskite. In the octahedral structure of the lead halide, Pb atoms are at the center of the halide octahedrons. The transmission electron microscopy (TEM) was applied to reveal the microstructure and chemical composition of materials. Herein, more detailed characterizations of perovskite nanoplatelets were also carried out using energy dispersive X-ray spectroscopy (EDX) and TEM to assess the structure, crystallinity, and elemental composition. We investigate the crystal structure transformations with a complete perovskite conversion process from PbI_2 into $CH_3NH_3PbI_3$. **Figure 2**a is a representative low resolution TEM image of the perovskite platelet. In Figure 2b–e the corresponding Pb, I, C, and N mapping images obtained by EDX, which confirms the whole hexagonal nanoplatelet is elemental-uniform with the perovskite conversion process. The crystal structure of the $CH_3NH_3PbI_3$ perovskite is evaluated by high resolution transmission electron microscopy (HRTEM) in Figure 2f, and inset is the corresponding fast Fourier transform pattern from this HRTEM image along the [—120] zone axis.

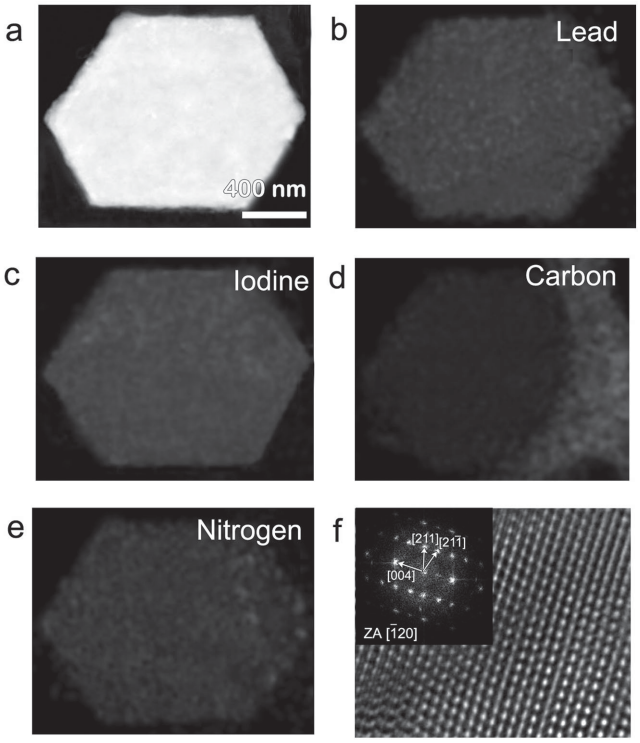

Figure 2. Electron microscopy characterization of the perovskite nanoplatelets. a) Low-resolution scanniong transmission electrion microscope (STEM) image of a perovskite nanoplatelet. b–e) Element mapping showing the uniformity of the perovskite nanoplatelets. f) High resolution transmission electron microscope (HRTEM) image showing the structure of the perovskite nanoplatelets. Inset is the corresponding fast Fourier transform (FFT) pattern along the [—120] zone axis (ZA).

2.2. Thickness-Dependent Raman Spectra of the Perovskite Nanoplatelets

Raman characterizations (mapping and spectroscopy) are commonly used as powerful tools to characterize materials, especially 2D materials, thanks to their unique advantages of relatively high spatial resolution, sensitive to the sample thickness, crystal structures, and electronic band structures, and so on. Raman imaging and spectroscopy characterization of the as-prepared perovskite nanoplatelets grown on Si/SiO_2 with the lateral dimension of about 10 μm and the thickness from 5 to 200 nm are shown in **Figure 3** and Figure S5 (Supporting Information). We observe clear signals of Raman peaks at ≈70, 95, and 110 cm^{-1} from Figure 3a,b. These three peaks are assigned to B_{2g}, degenerate A_{1g} and B_{1g}, and B_{3g}, respectively, as shown in Table S1 (Supporting Information).[40] In this article, it is more intriguing that all three modes exhibit well-defined thickness dependence for these perovskite nanoplatelets. The B_{2g} vibration softens from 74 to 70 cm^{-1} (red shifts), while the degenerate A_{1g} and B_{1g} vibration stiffens from 94 to

© 2016 WILEY-VCH Verlag GmbH & Co. KGaA, Weinheim

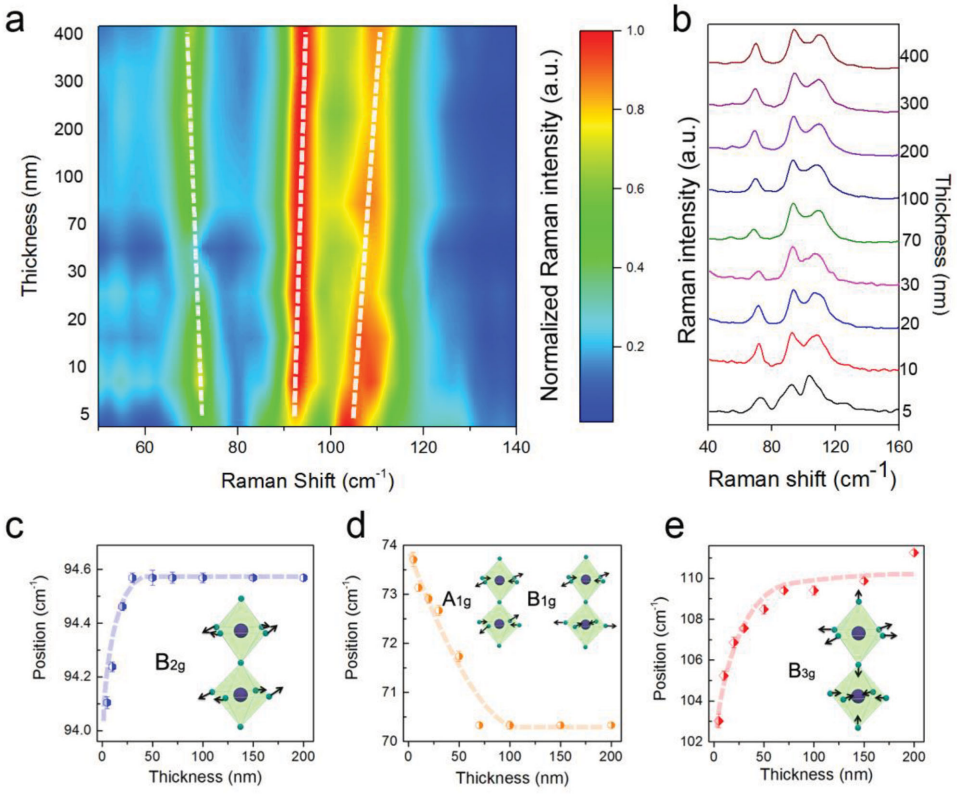

Figure 3. Raman spectra of the perovskite nanoplatelets and evolution of spectral features with thickness increase. a) Raman intensity map taken depending on the perovskite nanoplatelet thickness from 5 to 400 nm. b) Corresponding typical Raman spectra of the perovskite nanoplatelets with different thickness from 5 to 400 nm. In the measured spectroscopy range of 40–160 cm^{-1}, the Raman spectra reveal four distinct bands at 70, 95, and 110 cm^{-1} assigned to B_{2g}, degenerate A_{1g} and B_{1g}, and B_{3g}, respectively. c–e) Peak position evolution for the three Raman modes B_{2g}, degenerate A_{1g} and B_{1g}, and B_{3g} with the thickness increase. The inserts of (b–d) are schematic representations of these Raman modes of vibration of the PbI_3 in $CH_3NH_3PbI_3$. The excitation wavelength used for Raman measurements is 532 nm.

95 cm^{-1} (blue shifts) and the B_{3g} vibration stiffens from 103 to 110 cm^{-1} (blue shift) with increasing sample thickness. The peak positions of the three Raman modes show remarkable thickness dependence for the perovskite nanoplatelets with thickness below ≈50 nm (see Figure 3c–e), which could be due to the increase of interlayer interaction or the lattice distortion as the thickness increases or the surface defects in very thin perovskite nanoplatelets. Raman characterizations involved these sensitive thickness-dependent Raman peaks evolutions, which may provide a convenient and reliable method for identification of perovskite nanoplatelet thickness in the further Raman investigations for the perovskite nanoplatelets in the future. Moreover, Raman mapping further demonstrate that the intensity of degenerate A_{1g} and B_{1g} mode at 95 cm^{-1} and the B_{3g} mode at 110 cm^{-1} at the edge of the perovskite nanoplatelet show polarization-dependent behavior with the incident light. Figure S6 (Supporting Information) shows the optical images and corresponding Raman images of a perovskite nanoplatelet with different rotation angles of the nanoplatelet. The thickness of this perovskite nanoplatelet is 160 nm (Figure S7, Supporting Information). It can be seen from the Raman images of the intensity of degenerate A_{1g} and B_{1g} and B_{3g} modes that the perovskite nanoplatelets grown on Si/SiO_2 substrate is extremely homogenous. More intriguingly, we observed the polar phenomenon at the edge of the perovskite nanoplatelet by changing the nanoplatelet direction. The mechanism of this polar phenomenon at the edge of the perovskite nanoplatelet is still unclear, which will be further studied in detail in future work.

2.3. Thickness-Dependent Photoresponse and Mechanism of Perovskite Devices

With the high sensitivity of visible-light, organic-based lead halide perovskites attract wide attentions on the aspect of solar cell and photodetection applications.[8,11,22–27] Flakes with thickness ranging from 10 to 150 nm were chosen to fabricate photoresponse devices. Typical optical images of such flakes with different thickness are shown in Figure S8 (Supporting Information). For the fabrication of the electrodes, a copper grid was placed on top of as-grown flake as a shadow mask for resist-free metal evaporation. Cr/Au (5/50 nm) was used as contact metal via thermal evaporation deposition, and the distance between the two electrodes is 2–3 μm. The prepared samples are loaded in a vacuum probe station for all the following measurements. The current–voltage (I_d–V_d) characteristics were characterized in the dark and under 633 nm

© 2016 WILEY-VCH Verlag GmbH & Co. KGaA, Weinheim

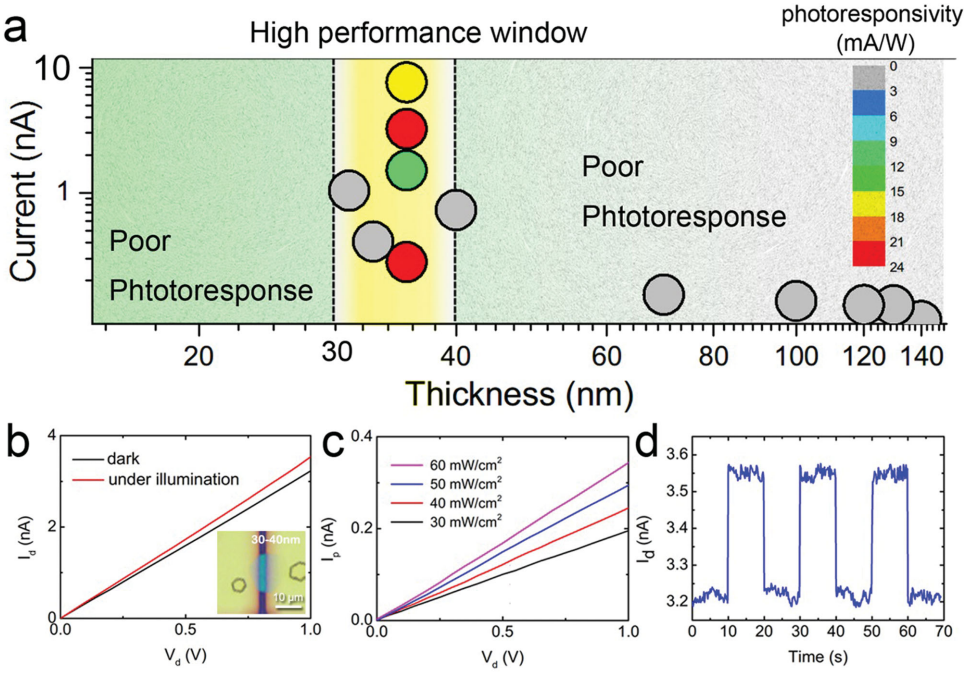

Figure 4. Photoresponse of perovskite device. a) Different electrical performances with perovskite nanoplatelets depending on different thickness. Derived bias is 1 V for both dark current and photoresponse. Laser illumination for photoresponse is 60 mW cm^{-2} 633 nm. b) Dark and 60 mW cm^{-2} laser illuminated *I–V* curves. c) Photocurrent under different laser powers. d) Time resolved photoresponse under 60 mW cm^{-2} illumination and 1 V bias.

laser illumination. As shown in **Figure 4**a, flakes with different thickness demonstrate totally different performances, and all the data are derived at 1 V bias (for both dark current and photoresponse) and under 60 mW cm^{-2} 633 nm laser illumination (for photoresponse). For the samples as thin as ≈10 nm, the devices do not work at all, i.e., no detectable current can be obtained both in the dark and under illumination. The dark current is about 100 pA for the flakes with a thickness in the 70–150 nm range at a bias of 1 V, but no photoresponse can be detected for these relatively thick samples. Interestingly, 30–40 nm thick samples behave the best electronic and optoelectronic performances, so we focus our measurement on these samples. The dark current shows a distribution over a range from ≈200 pA to ≈10 nA, and obvious photoresponse was obtained from most of these devices with a responsivity between about 10 and 25 mA W^{-1}.

The photoresponse performances of a typical device based on a 35 nm thick flake is shown in Figure 4b–d. As shown in Figure 4b, the *I–V* curve in the dark demonstrates a linear behavior within applied bias range (from −1 to 1 V), indicating ohmic contact has formed between the sample and the electrodes. Different from the insulator like performance for PdI_2 based perovskite synthesized by solution process,[24,41,42] our samples have a much lower resistance in the dark state, which can ascribe to the solution-free process. Optical image of such simple metal–semiconductors–metal (MSM) structure is shown as the inset. An obvious photoresponse was observed for our MSM device (red line in **Figure 5**b), and ≈0.35 nA photocurrent was obtained under 60 mW cm^{-2} illumination at 1 V bias, resulting in a photoresponsivity ≈23.3 mA W^{-1}. More detailed measurements were carried out to evaluate the photodetection performances. The photocurrent (current under illumination minus dark current) is tested under different incident laser power densities in the 30–60 mW cm^{-2} range, as shown in Figure 4c. The current increases linearly with the incident power density, and the saturation of the photocurrent is not reached under the applied experimental conditions. The stability of the photocurrent is shown in Figure 4d. Our sample demonstrates a stable on/off behavior with the switch of the incident laser, and both the rise and decay times for the on–off current under illumination are ≈150 ms.

To investigate the mechanism of thickness dependent photoresponse for the perovskite devices, we further investigate the thickness-dependent optical properties corresponding to photoresponse for the perovskite devices. We measured the photoluminescence (PL) spectra and time-resolved PL spectra of the perovskite nanoplatelets with different thickness, as shown in Figure 5. In Figure 5a, the optical images of perovskite platelets with different thickness are exhibited with different color. From samples S1 to S6, the thicknesses of perovskite platelets are 20, 30, 50, 70, 100, and 150 nm, respectively. The PL spectra measured from samples S1 to S6 are shown in Figure 5b. The excitation wavelength is 400 nm with a laser spot of ≈50 μm, which can cover the whole sample region. The emission wavelength located at around 760 nm, which is attributed to the band edge emission of $CH_3NH_3PbI_3$. The PL intensity increases with increasing the thickness of perovskite from 20 to 150 nm. Assuming the quantum yield of these samples are the same, the strong intensity of PL means more absorption of excitation laser source with thick samples. However, the photoresponse measurement results suggest that only sample

© 2016 WILEY-VCH Verlag GmbH & Co. KGaA, Weinheim

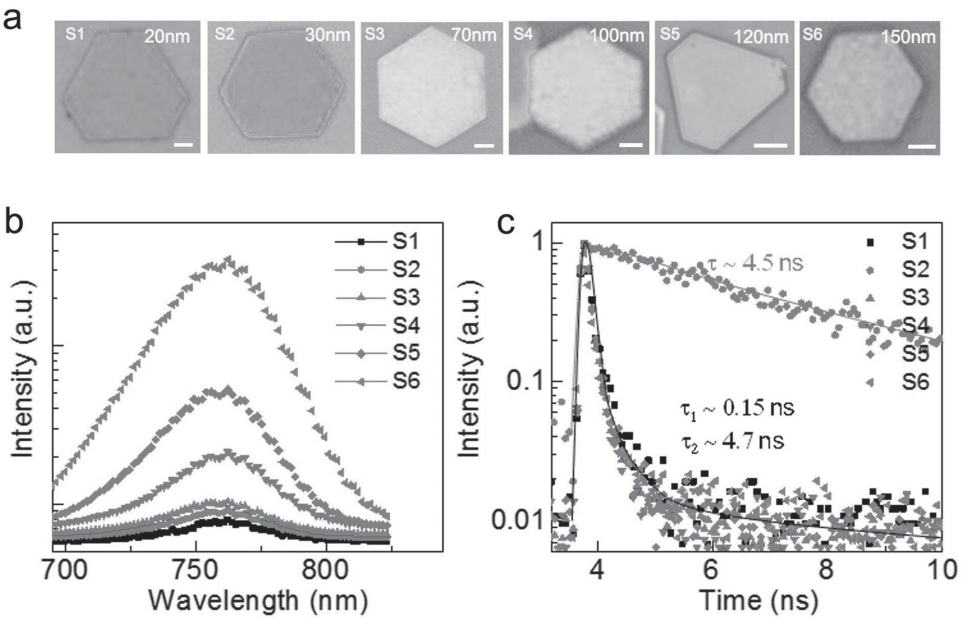

Figure 5. Photoluminescence of the perovskite nanoplatelet depending on different thickness. a) Optical images of perovskite grown on Si/SiO_2. Their colors correspond to different thickness as determined by AFM height topography. b) Comparison of the PL spectra measured from S1 to S5, respectively. The PL intensity increases with increasing the thickness of perovskite from 20 to 150 nm. c) Time resolved PL decay transients measured at 760 ± 10 nm for perovskites with different thickness. The decay profiles of sample S1 to S6 with emission wavelength of 760 nm are plotted. For sample S1 (thickness of ≈30 nm), the experimental data can be fitted with one lifetime of ≈4.5 ns. For sample S2 to S5, they share almost the same two lifetime components – the short lifetime τ_1 (≈0.15 ns) and the long lifetime (≈4.7 ns). All the PL spectra/images were recorded under an excitation laser of 532 nm. Scale bar is 2 μm.

with thickness of 30 nm (as shown in Figure 4) exhibited the best performance compared to the counterparts with larger thickness. For the photoresponse measurement, the larger current with light on means more electrons and holes generated, separated, and collected by the two different electrodes. Therefore, the longer lifetime of photogenerated carriers is vital for the photoresponse performance. In Figure 5c, the decay profiles of samples S1 to S6 with emission wavelength of 760 nm are plotted. For sample S2 (thickness of ≈30 nm), the experimental data can be fitted with one lifetime of ≈4.5 ns, which is consistent with previous reports. However, for samples S1, S3 to S6, they share almost the same two lifetime components – the short lifetime τ_1 (≈0.15 ns) and the long lifetime (≈4.7 ns). The long lifetime component of ≈4.7 ns is similar to the lifetime of S1 (≈4.5 ns), which is attributed to the recombination rate of carriers near the band edge. On the other hand, the short lifetime of ≈0.15 ns in perovskite is related to the surface taps, defects, or self-absorption. The dominant short lifetime component (≈93%) in S1, S3 to S6 is detrimental to the photoresponse in the perovskite based photodetectors. As to the different recombination lifetimes of perovskite with different thickness, two possible reasons can be included: (1) the pervoskite platelets with thickness ≈30–40 nm have the best crystal quality compared with other thicker perovskite, where more quenching centers exist; (2) Considering the absorption coefficient of pervoskite, the penetration depth of laser at wavelength 532 nm is around 30–40 nm. It means that reabsorption should be play an important role in thicker perovskite platelet. A new quenching channel occurs, leading to a fast recombination process. Consequently, in sample S2 with thickness of ≈30 nm, owing to its dominant long lifetime (≈4.5 ns) indicates the good property for photoresponse, thus leading to the good performance of sample S1, as shown in Figure 4.

3. Conclusion

In this work we explore the lead halide perovskite nanoplatelet growth on SiO_2/Si substrates by using a simple two-step vapor transport chemical deposition method. And more significantly, by this method we could control the perovskite crystal thickness under diverse synthesis conditions and further investigate their crystal quality and functional characterizations, closely related with the photoresponse, optoelectronic, and photovoltaic applications and device performance. The photoresponse measurement results suggest that the sample with thickness of around 30 nm exhibited the best performance compared to the counterparts with smaller or larger thickness, thus coinciding to the result of photodetection performance measurement. Synthesis of high quality perovskite crystal with controlled thickness could be a key point for the fundamental investigation of the intrinsic photoresponse and optoelectronic properties of perovskite materials.

4. Experimental Section

Synthesis of Lead Halide Platelets: PbI_2 powder (99.999%, Aldrich) was used as a single source and put into a quartz tube mounted on a single-zone furnace (XST split tube furnaces, Thermcraft, Inc.). The freshly Si/

© 2016 WILEY-VCH Verlag GmbH & Co. KGaA, Weinheim

SiO_2 substrate (1 cm × 3 cm) was placed in the best location inside the quartz tube as shown in Figure S1 (Supporting Information). The quartz tube was first evacuated to a base pressure of 3 mTorr, followed by a 40 sccm flow of high purity Ar gas. The pressure and temperature in the quartz tube were controlled and stabilized to desired values (360 °C and 30 Torr). For all lead halide platelets, the synthesis progress was carried out within 20 min and the furnace was allowed to cool down naturally to ambient temperature.

Synthesis of CH_3NH_3I: 18.0 mL of methylamine (40 wt% in water, Sigma) was dissolved in 100 mL of absolute ethanol (Absolute for analysis, Merck Millipores) in a 250 mL round bottom flask. 20.0 mL of hydroiodic acid (57 wt% in water, Alfa Aesar) was added into the solution dropwise. After that, the solution was stirred at 0 °C for 2 h. The raw product was obtained by removing the solvents using a rotary evaporator. A recrystallization process of the raw product, including the redissolution in 80 mL absolute ethanol and the precipitation after the addition of 300 mL diethyl ether, was carried out twice to get a much purer product. Finally, the white color powders were collected and dried at 60 °C for 24 h in a vaccum oven.

Synthesis of Perovskites via the Reaction with CH_3NH_3I and PbI_2: The reactions were done using the similar CVD system as the synthesis part of the lead halide nanoplatelets. CH_3NH_3I was used as a source and placed in the center of the quartz tube while Si/SiO_2 substrate with as-grown lead halide platelets were placed around 25–30 cm away from the center in the downstream region. The quartz tube was first evacuated to a base pressure of 3 mTorr, followed by a 40 sccm flow of high purity Ar gas. The pressure was then stabilized to 30 Torr and the temperature was elevated to 120 °C. The reaction progress was kept there for 2 h and then the furnace was allowed to cool down naturally to ambient temperature.

XRD Measurement: X-ray diffraction pattern (2θ scans) of perovskite nanoplatelets on the SiO_2/Si substrates were obtained by using an X-ray diffractometer (XRD Shimadzu thin film), with Cu-K_α radiation ($\lambda = 1.54050$ Å) within a diffraction angle (2θ) from 5° to 60°.

AFM Measurement: The AFM images were measured by using Dimension Fastscan SPM system (Bruker, USA) with tapping mode under ambient conditions. All the experiments used commercial silicon tips with resonant frequency of 300 kHz and a nominal spring constant of 40 N m^{-1}.

SEM Measurement: All the SEM images were measured by using JEOL JEM7600F under an accelerating voltage of 10 kV.

TEM Measurement: The PbI_2 nanoplatelets were flaked off from the SiO_2/Si substrates by using Toluene (99.85%, Acros Organics) and then transferred onto the TEM grids (Quantifoil Mo grids). PbI_2 samples on the TEM grids were converted into $CH_3NH_3PbI_3$ perovskite nanoplatelets by using the same method in the perovskite synthesis part above. The HRTEM was performed by using a FEI Tecnai F20 operated with an acceleration voltage of 200 kV. The chemical compositions of $CH_3NH_3PbI_3$ perovskite nanoplatelets were determined by EDX attached to FEI Tecnai F20.

Raman and PL Measurement: All the PL and Raman spectra were measured by using a WITec alpha300 RAS Raman system with a piezo crystal controlled scanning stage, an objective lens of 100× magnification (numerical aperture = 0.95), and an electron multiplying charge-coupled device (CCD). PL spectra were collected by using a 600 lines per mm grating. Raman spectra with low-frequency Raman modes and good spectral resolutions were collected by using a low-wavenumber coupler and a 2400 lines per mm grating. All the Raman and PL spectra were recorded under an excitation laser of 532 nm (E_{laser} = 2.33 eV). The laser spot was of ≈500 nm in diameter. To avoid the laser-induced heating, laser power was kept below 0.1 mW. The PL emission signal was collected in a standard backscattering geometry and dispersed by a 0.25 m DK240 spectrometer with 150 g mm^{-1} grating. The emission signal was time-resolved using an Optoscope streak camera system that has an ultimate temporal resolution of ≈10 ps.

Device Fabrication and Characterization: Copper grid was placed on top of as-grown flake as a shadow mask for resist-free metal evaporation. Cr/Au (5/50 nm) was used as contact metal via thermal evaporation deposition. As- prepared devices were loaded in a vacuum probe station for all the electronic and optoelectronic measurements. DC electrical measurements were performed using Agilent B1500A. 633 nm was used as the excitation source for photocurrent test.

Supporting Information

Supporting Information is available from the Wiley Online Library or from the author.

Acknowledgements

This work was supported by the Singapore National Research Foundation (NRF) under RF Award No. NRF-RF2013-08, the start-up funding from Nanyang Technological University (M4081137.070) and M4080514, and the Ministry of Education AcRF Tier 2 grants MOE2013-T2-1-081 and MOE2014-T2-1-044. X.L. thanks the support from the 100-Talents Program of the Chinese Academy of Sciences (No.Y5862911ZX). C.C. and T.Y. thank the support of Ministry of Education AcRF Tier 2 grants MOE2012-T2-2-049 and Tier 1 grants RG110/15. C.W. and C.J. thank the Center for Electron Microscopy of Zhejiang University for the access to TEM facilities, and the financial support from the National Science Foundation of China (51222202 and 51472215), the National Basic Research Program of China (2014CB932500 and 2015CB921000), and the Fundamental Research Funds for the Central Universities (2014XZZX003-07).

Received: March 18, 2016
Published online: May 25, 2016

[1] M. M. Lee, J. Teuscher, T. Miyasaka, T. N. Murakami, H. J. Snaith, *Science* **2012**, *338*, 643.
[2] J. Burschka, N. Pellet, S. J. Moon, R. Humphry-Baker, P. Gao, M. K. Nazeeruddin, M. Gratzel, *Nature* **2013**, *499*, 316.
[3] B. Cai, Y. D. Xing, Z. Yang, W. H. Zhang, J. S. Qiu, *Energy Environ. Sci.* **2013**, *6*, 1480.
[4] L. Etgar, P. Gao, Z. S. Xue, Q. Peng, A. K. Chandiran, B. Liu, M. K. Nazeeruddin, M. Gratzel, *J. Am. Chem. Soc.* **2012**, *134*, 17396.
[5] J. H. Heo, S. H. Im, J. H. Noh, T. N. Mandal, C. S. Lim, J. A. Chang, Y. H. Lee, H. J. Kim, A. Sarkar, M. K. Nazeeruddin, M. Gratzel, S. I. Seok, *Nat. Photonics* **2013**, *7*, 487.
[6] A. Kojima, K. Teshima, Y. Shirai, T. Miyasaka, *J. Am. Chem. Soc.* **2009**, *131*, 6050.
[7] M. Liu, M. B. Johnston, H. J. Snaith, *Nature* **2013**, *501*, 395.
[8] W. Nie, H. Tsai, R. Asadpour, J. C. Blancon, A. J. Neukirch, G. Gupta, J. J. Crochet, M. Chhowalla, S. Tretiak, M. A. Alam, H. L. Wang, A. D. Mohite, *Science* **2015**, *347*, 522.
[9] J. H. Noh, S. H. Im, J. H. Heo, T. N. Mandal, S. I. Seok, *Nano Lett.* **2013**, *13*, 1764.
[10] G. C. Xing, N. Mathews, S. Y. Sun, S. S. Lim, Y. M. Lam, M. Gratzel, S. Mhaisalkar, T. C. Sum, *Science* **2013**, *342*, 344.
[11] W. S. Yang, J. H. Noh, N. J. Jeon, Y. C. Kim, S. Ryu, J. Seo, S. I. Seok, *Science* **2015**, *348*, 1234.
[12] H. M. Zhu, Y. P. Fu, F. Meng, X. X. Wu, Z. Z. Gong, Q. Ding, M. V. Gustafsson, M. T. Trinh, S. Jin, X. Y. Zhu, *Nat. Mater.* **2015**, *14*, 636.
[13] K. Chondroudis, D. B. Mitzi, *Chem. Mater.* **1999**, *11*, 3028.
[14] T. Hattori, T. Taira, M. Era, T. Tsutsui, S. Saito, *Chem. Phys. Lett.* **1996**, *254*, 103.
[15] C. R. Kagan, D. B. Mitzi, C. D. Dimitrakopoulos, *Science* **1999**, *286*, 945.

© 2016 WILEY-VCH Verlag GmbH & Co. KGaA, Weinheim

[16] L. C. Schmidt, A. Pertegas, S. Gonzalez-Carrero, O. Malinkiewicz, S. Agouram, G. M. Espallargas, H. J. Bolink, R. E. Galian, J. Perez-Prieto, *J. Am. Chem. Soc.* **2014**, *136*, 850.
[17] S. D. Stranks, G. E. Eperon, G. Grancini, C. Menelaou, M. J. P. Alcocer, T. Leijtens, L. M. Herz, A. Petrozza, H. J. Snaith, *Science* **2013**, *342*, 341.
[18] P. Docampo, J. M. Ball, M. Darwich, G. E. Eperon, H. J. Snaith, *Nat. Commun.* **2013**, *4*, 2761.
[19] H. S. Kim, C. R. Lee, J. H. Im, K. B. Lee, T. Moehl, A. Marchioro, S. J. Moon, R. Humphry-Baker, J. H. Yum, J. E. Moser, M. Gratzel, N. G. Park, *Sci. Rep.* **2012**, *2*, 1.
[20] N. G. Park, *J. Phys. Chem. Lett.* **2013**, *4*, 2423.
[21] G. E. Eperon, V. M. Burlakov, P. Docampo, A. Goriely, H. J. Snaith, *Adv. Funct. Mater.* **2014**, *24*, 151.
[22] Y. C. Liu, Z. Yang, D. Cui, X. D. Ren, J. K. Sun, X. J. Liu, J. R. Zhang, Q. B. Wei, H. B. Fan, F. Y. Yu, X. Zhang, C. M. Zhao, S. Z. Liu, *Adv. Mater.* **2015**, *27*, 5176.
[23] Y. P. Fu, F. Meng, M. B. Rowley, B. J. Thompson, M. J. Shearer, D. W. Ma, R. J. Hamers, J. C. Wright, S. Jin, *J. Am. Chem. Soc.* **2015**, *137*, 5810.
[24] G. Wang, D. Li, H. C. Cheng, Y. Li, C. Y. Chen, A. Yin, Z. Zhao, Z. Lin, H. Wu, Q. He, M. N. Ding, Y. Liu, Y. Huang, X. F. Duan, *Sci. Adv.* **2015**, *1*, e1500613.
[25] E. Horvath, M. Spina, Z. Szekrenyes, K. Kamaras, R. Gaal, D. Gachet, L. Forro, *Nano Lett.* **2014**, *14*, 6761.
[26] P. Qin, A. L. Domanski, A. K. Chandiran, R. Berger, H. J. Butt, M. I. Dar, T. Moehl, N. Tetreault, P. Gao, S. Ahmad, M. K. Nazeeruddin, M. Gratzel, *Nanoscale* **2014**, *6*, 1508.
[27] J. N. Chen, S. S. Zhou, S. Y. Jin, H. Q. Li, T. Y. Zhai, *J. Mater. Chem. C* **2016**, *4*, 11.
[28] P. Gao, M. Gratzel, M. K. Nazeeruddin, *Energy Environ. Sci.* **2014**, *7*, 2448.
[29] S. Kazim, M. K. Nazeeruddin, M. Gratzel, S. Ahmad, *Angew. Chem., Int. Ed.* **2014**, *53*, 2812.
[30] N. Pellet, P. Gao, G. Gregori, T. Y. Yang, M. K. Nazeeruddin, J. Maier, M. Gratzel, *Angew. Chem., Int. Ed.* **2014**, *53*, 3151.
[31] G. Grancini, A. R. S. Kandada, J. M. Frost, A. J. Barker, M. De Bastiani, M. Gandini, S. Marras, G. Lanzani, A. Walsh, A. Petrozza, *Nat. Photonics* **2015**, *9*, 695.
[32] C. Zhang, D. Sun, C. X. Sheng, Y. X. Zhai, K. Mielczarek, A. Zakhidov, Z. V. Vardeny, *Nat. Phys.* **2015**, *11*, 428.
[33] H. C. Cho, S. H. Jeong, M. H. Park, Y. H. Kim, C. Wolf, C. L. Lee, J. H. Heo, A. Sadhanala, N. Myoung, S. Yoo, S. H. Im, R. H. Friend, T. W. Lee, *Science* **2015**, *350*, 1222.
[34] D. B. Mitzi, *Chem. Mater.* **2001**, *13*, 3283.
[35] S. T. Ha, X. F. Liu, Q. Zhang, D. Giovanni, T. C. Sum, Q. H. Xiong, *Adv. Opt. Mater.* **2014**, *2*, 838.
[36] Q. Zhang, S. T. Ha, X. F. Liu, T. C. Sum, Q. H. Xiong, *Nano Lett.* **2014**, *14*, 5995.
[37] X. F. Liu, S. T. Ha, Q. Zhang, M. de la Mata, C. Magen, J. Arbiol, T. C. Sum, Q. H. Xiong, *ACS Nano* **2015**, *9*, 687.
[38] Z. Zheng, A. Liu, S. Wang, Y. Wang, Z. Li, W. M. Lau, L. Zhang, *J. Mater. Chem.* **2005**, *15*, 4555.
[39] T. Baikie, Y. Fang, J. M. Kadro, M. Schreyer, F. Wei, S. G. Mhaisalkar, M. Graetzel, T. J. White, *J. Mater. Chem. A* **2013**, *1*, 5628.
[40] M. A. Pérez-Osorio, R. L. Milot, M. R. Filip, J. B. Patel, L. M. Herz, M. B. Johnston, F. Giustino, *J. Phys. Chem. C* **2015**, *119*, 25703.
[41] E. Horváth, M. Spina, Z. Szekrényes, K. Kamarás, R. Gaal, D. Gachet, L. Forró, *Nano Lett.* **2014**, *14*, 6761.
[42] F. Li, C. Ma, H. Wang, W. Hu, W. Yu, A. D. Sheikh, T. Wu, *Nat. Commun.* **2015**, *6*, 8238.

© 2016 WILEY-VCH Verlag GmbH & Co. KGaA, Weinheim